Effect of Tempering on the Microstructure and Tensile Properties of a Martensitic Medium-Mn Lightweight Steel

SUKJIN LEE, SEOK-HYEON KANG, JAE-HOON NAM, SANG-MIN LEE, JAE-BOK SEOL, and YOUNG-KOOK LEE

In the present study a Fe-8.8Mn-5.1Al-0.31C (wt pct) medium-Mn lightweight steel with martensitic matrix was newly designed, and the effect of tempering on its microstructure and tensile properties was investigated. When the medium-Mn lightweight steel specimen was quenched from annealing temperature of 1373 K (1100 °C), it revealed a triple-phase microstructure consisting of 64.6 pct fresh martensite, 20.2 pct ferrite, and 15.2 pct retained austenite. Tempering the as-quenched specimen at temperatures less than 573 K (300 °C) induced the precipitation of thin cementite or κ-carbide platelets in tempered martensite. With the increasing tempering temperature, the type of precipitate changed from cementite to κ-carbide, and thickening of platelets with the longer interspacing was observed by means of transmission electron microscopy and atom probe tomography. While the as-quenched specimen revealed high strain-hardening rate (SHR) and poor elongation (< 2 pct), tempered specimens exhibited moderate SHR and improved elongation (> 16.8 pct) mainly due to gradual transformation-induced plasticity in retained austenite stabilized by tempering. In particular, the 373 K (100 °C)-tempered specimen with tempered martensite embedded with thin cementite platelets revealed ultrahigh strengths (yield strength of 945 MPa and ultimate tensile strength of ~ 1.56 GPa) with moderate elongation of ~ 16.8 pct.

I. INTRODUCTION

IMPROVEMENTS of both fuel efficiency and passenger safety of vehicles can be achieved by employing high-strength lightweight steels with ultimate tensile strength (UTS) above 1.0 GPa. To obtain ultrahigh strength alongside moderate ductility, various strengthening mechanisms, such as grain refinement, dislocation hardening, TRansformation-Induced Plasticity (TRIP) and TWinning-Induced Plasticity (TWIP), and their coupling, have been studied.[1–6] To reduce the weight of steel, a large amount of Al (> 5 wt pct) is added as a lightweight alloying element.[7–38]

The high-strength lightweight steels reported until now can be categorized into four groups based on their matrix microstructure: austenite, ferrite, ferrite + austenite (dual-phase), and ferrite + austenite + martensite (triple-phase). As shown in Table I, high-Mn austenitic lightweight steels are generally stronger (UTS > 1.0 GPa) and lighter than medium-Mn ferritic, dual-phase, and triple-phase lightweight steels. For example, Kim et al.[20] reported that high UTS (~ 1.55 GPa) and high specific UTS (SUTS = 227 MPa $(gcm^{-3})^{-1}$) could be obtained in an Fe-16.1Mn-9.6Al-0.86C-4.9Ni (wt pct) austenitic lightweight steel by controlling the distribution and morphology of Fe-Al type brittle intermetallic compounds (B2) in the austenite matrix. However, because austenitic lightweight steels have a high amount of alloying elements (Mn and Ni) and high material cost, and also undergo difficult fabrication processes,[7–20] medium-Mn lightweight steels with Mn concentration less than 10 wt pct are more attractive.[21–38] When Mn concentration is less than 10 wt pct, matrix microstructure changes from austenite to ferrite, dual-phase or triple-phase. Ferritic medium-Mn lightweight steels exhibit yield strength

SUKJIN LEE is with the Department of Materials Science and Engineering, Yonsei University, Seoul, 03722, Republic of Korea and also with the ASPPRC, Colorado School of Mine, Golden, CO 80401. SEOK-HYEON KANG, JAE-HOON NAM, and YOUNG-KOOK LEE are with the Department of Materials Science and Engineering, Yonsei University. Contact e-mail: yklee@yonsei.ac.kr SANG-MIN LEE is with the Department of Materials Science and Engineering, Yonsei University and also with the Sheet Productions Design Team, R&D Center, Hyundai Steel, Dangjin, 31719, Republic of Korea. JAE-BOK SEOL is with National Institute for Nanomaterials Technology, POSTECH, Pohang, 37673, Republic of Korea.

Table I. Chemical Compositions and Tensile Properties of Various Lightweight Steels Categorized by Their Matrix Microstructure

Matrix Microstructure	Chemical Composition (Weight Percent)				Tensile Properties			
	Mn	Al	C	Ni	YS (MPa)	UTS (MPa)	El (Pct)	References
Austenite (+ κ-Carbide)	12.0–30.0	5.0–12.0	0.6–2.00	5.0	355–1355	620–1545	20.0–98.0	7–20
Ferrite (+ κ-Carbide)	2.0–6.0	4.0–8.0	0.1–0.7	—	565–762	638–979	7.6–36.0	21–26
Ferrite + Austenite (+ κ-Carbide)	3.0–12.0	5.0–10.0	0.2–1.2	—	561–685	771–920	32.0–58.1	27–35
Ferrite + Austenite + Martensite (+ κ-Carbide)	9.0–10.0	5.0–6.5	0.15–0.25	—	600	808	43.0	36–38

(YS) of 580-760 MPa and UTS of 630-980 MPa, which are similar to those of dual-phase and triple-phase medium-Mn lightweight steels. However, the elongation (El) of ferritic steels is poor (Table I). Dual-phase and triple-phase medium-Mn lightweight steels have neither YS above 700 MPa nor UTS above 1.0 GPa; the strengths of these steels are lower than those of high-Mn austenitic lightweight steel, TRIP steel, and TWIP steel.

Therefore, in the present study alloy design was performed with a new concept in which medium-Mn lightweight steel has a hard martensitic matrix. The effect of tempering of martensite on the microstructure and tensile properties of the steel was also investigated according to tempering temperature.

II. MATERIAL AND METHODS

A lightweight steel ingot with a chemical composition of Fe-8.8Mn-5.1Al-0.31C (wt pct) was fabricated by vacuum-induction melting. The ~30 kg ingot was homogenized at 1473 K (1200 °C) for 2 hours, hot-rolled to a ~3 mm thick plate above 1173 K (900 °C), isothermally held at 923 K (650 °C) for 1 hour for simulating coiling procedure, and furnace-cooled to room temperature. Specimens for dilatometry and tensile testing were machined along the longitudinal direction of the hot-rolled plate.

Dilatometric specimens measuring $3 \times 1 \times 10$ mm³ were annealed at 1373 K (1100 °C) for 15 minutes in a vacuum atmosphere of ~ 1×10^{-6} torr, gas-quenched to room temperature, tempered in the temperature range of 373-573 K (100-300 °C) for 100 minutes, and finally gas-quenched to room temperature again using a quench dilatometer (Theta, Dilatronic III). The dilatometric specimens were mechanically and electrochemically polished, and then etched using the Viella's solution (45 ml glycerol, 15 ml HNO_3, and 30 mL HCl). The microstructures of annealed and tempered specimens were observed using an optical microscope (OM; Olympus, BX41M), a field-emission scanning electron microscope (FE-SEM; JEOL, JSM-7001F) attached with electron backscattered diffraction (EBSD; EDAX-TSL, Digiview), and a field-emission transmission electron microscope (FE-TEM; JEOL, JEM-2100F). Thin foils were prepared using a focused ion beam (FIB; ZEISS, Crossbeam 540), and were

observed using the TEM operated at an acceleration voltage of 200 kV. The step size for SEM-EBSD observation was 0.2 μm.

The hardness tests of various phases were performed with a triangle-cone-type indenter and a load of 3 g using an ultramicro-Vickers hardness tester (DUH-W201S, Shimadzu). ASTM E8 subsized tensile specimens with a gauge portion 6 mm wide, 32 mm long, and 2.6 mm thick were annealed, water-quenched, and tempered like dilatometric specimens, and then deformed at an initial strain rate of 1×10^{-4} s⁻¹ using a universal testing machine (Instron, 3382). Changes in phase constituents before and after tensile tests were examined using a high-resolution X-ray diffractometer (HR-XRD; RIGAKU, SmartLab) with a Cu target. The scan rate and step size were 2 deg minutes⁻¹ and 0.02 deg, respectively. The fraction of retained austenite was calculated *via* the integrated intensity method.[39]

Samples for atom probe tomography (APT) were prepared by dual-beam FIB (FEI, Helios Nano-Lab 600). APT experiments were conducted using a local electrode atom probe (LEAP 4000X HR, CAME-CATM) in a voltage-pulsing mode. The experimental parameters were set to maintain a 0.5 pct detection rate, 20 pct pulse fraction and 200 kHz pulse repetition. All measurements were performed at − 223 °C (50 K) at a pressure less than 1×10^{-7} Pa. At least, two or more successful measurements were performed and evaluated, two of which contained more than 80 million ions. The APT data were visualized using IVAS software (version 3.6.14) by Cameca Instruments. The concentrations of C at 24 Da in an APT mass spectrum were measured using the peak decomposition algorithm of IVAS. Statistical errors for measured atom counts were calculated as $\sigma = (C_i \times (1 - C_i)/N)^{-1/2}$, where C_i corresponds to the measured atomic concentration of individual element i, and N is the total number of atoms collected in a bin.

III. RESULTS AND DISCUSSION

Figure 1 shows an equilibrium phase fraction *vs* temperature diagram of steel used, which was calculated using Thermo-Calc software and TCFE9 database.[40,41] The equilibrium fractions of austenite and ferrite at ~ 1273 K (1000 °C) are ~80 and ~20 pct, respectively. Cementite and κ-carbide start to precipitate at ~ 893 K

(620 °C) and ~ 483 K (210 °C), respectively, and their total equilibrium fraction is less than 6 pct. Therefore, it is expected that the transition of ~ 80 pct high-temperature austenite to martensite would occur during quenching from annealing temperature to room temperature. Martensite would bear high strength and ~ 20 pct ferrite would ensure ductility. In addition, tempering of martensite would cause the precipitation of
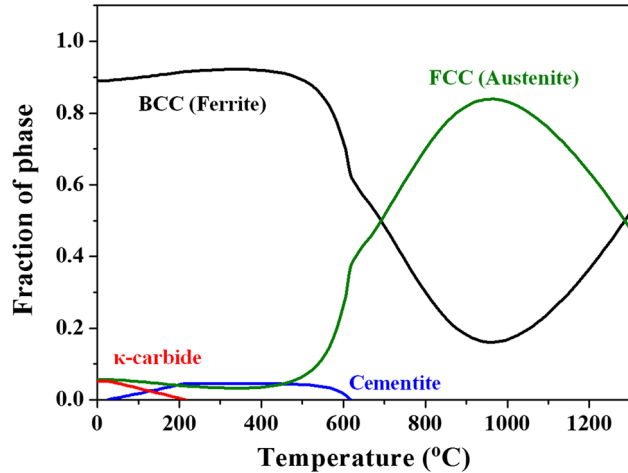

Fig. 1—Equilibrium phase fraction *vs* temperature diagram of Fe-8.8Mn-5.1Al-0.31C (wt pct) steel, calculated using Thermo-Calc software and TCFE9 database. The equilibrium fraction of austenite is at its maximum at 1223 K (950 °C). Cementite and κ-carbide start to precipitate at 893 K (620 °C) and 483 K (210 °C), respectively.

nanosized cementite and/or κ-carbide, resulting in ultrahigh UTS (above 1.5 GPa) with moderate ductility.

Figure 2(a) exhibits a light-optical microstructure of specimen annealed at 1373 K (1100 °C) for 15 minutes. The microstructure was composed of triple phases: α'-martensite (gray), retained γ-austenite (orange), and δ-ferrite (white). The average fraction of ferrite was measured by image analysis of five optical micrographs including Figure 2(a). The fraction of retained austenite was calculated using XRD pattern, and the remaining fraction was considered to be the martensite fraction. The average fractions of martensite, austenite, and ferrite are 64.6 pct, 15.2 pct, and 20.2 pct, respectively (Table II), which match well with the equilibrium fractions of austenite (77 pct) and ferrite (23 pct) at 1373 K (1100 °C) (Figure 1). The annealed specimens were tempered for 100 minutes at 373 K (100 °C), 473 K (200 °C), and 573 K (300 °C). All tempered specimens consisted of tempered martensite (α'_T), retained austenite, and ferrite; each phase fraction was almost unchanged by tempering (Table II). For detailed microstructural analysis, annealed and tempered specimens were observed again using SEM. Whereas the annealed specimen revealed martensite laths without any precipitates (Figure 2(b)), the 373 K (100 °C)-, 473 K (200 °C)-, and 573 K (300 °C)-tempered specimens showed fine platelets inside martensite laths (Figures 2(c) through (e)). The sizes of precipitates increased with increasing tempering temperature: precipitates were 15-30 nm thick and 300-800 nm long for the 373 K (100 °C)-tempered specimen and 150-200 nm
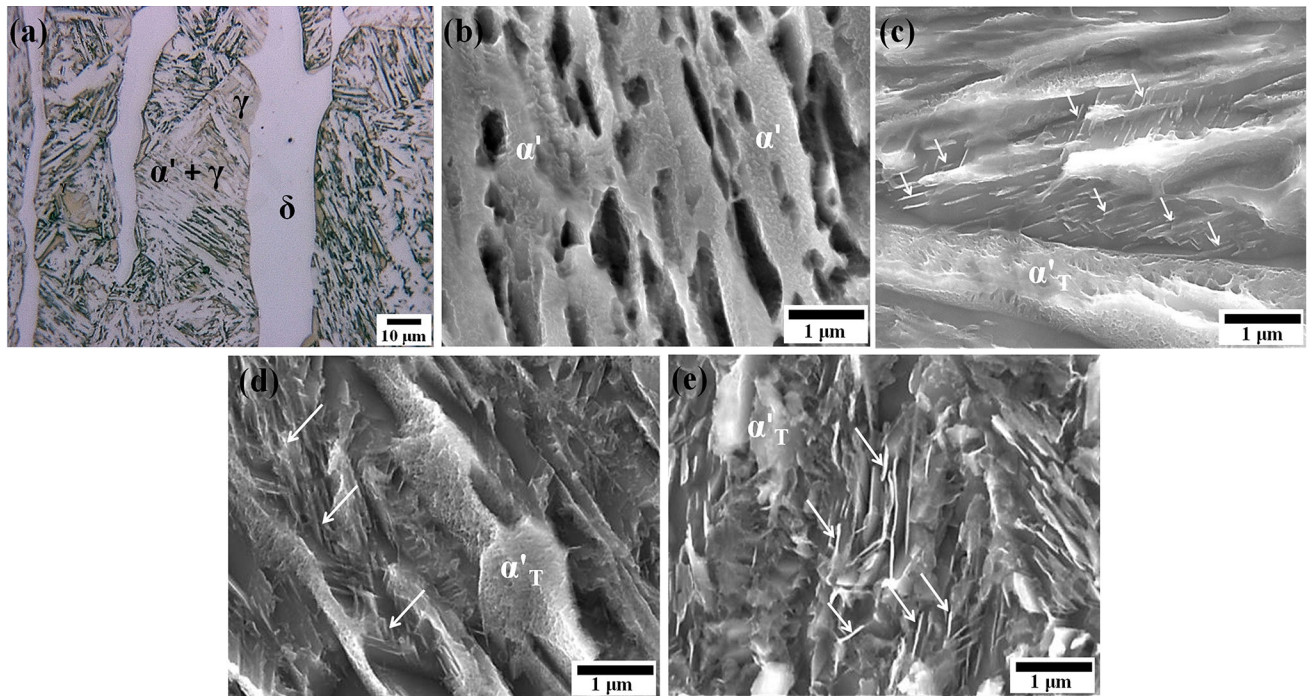

Fig. 2—Optical micrographs of (*a*) annealed specimen and SEM micrographs of (*b*) annealed, (c) 373 K (100 °C)-, (*d*) 473 K (200 °C)-, and (*e*) 573 K (300 °C)-tempered specimens. In the optical micrographs, it can be seen that all specimens have a triple-phase microstructure composed of α'-martensite (gray), γ-austenite (orange), and δ-ferrite (white). However, in the SEM micrographs, fine precipitates are observed inside martensite laths of tempered specimens.

Table II. Volume Fractions of Martensite, Austenite, and Ferrite Phases Before and After Tensile Tests in Annealed and Tempered Specimens

Specimen	Volume Fraction (Pct)		
	Martensite	Austenite	Ferrite
Annealed	64.6 ± 3.0 (75.7 ± 2.4)	15.2 ± 1.2 (4.1 ± 0.6)	20.2 ± 1.8 (20.2 ± 1.8)
373 K (100 °C)-Tempered	62.8 ± 2.9 (74.4 ± 2.9)	16.2 ± 0.8 (4.6 ± 0.7)	21.0 ± 2.1 (21.0 ± 2.1)
473 K (200 °C)-Tempered	63.3 ± 4.2 (75.5 ± 3.7)	16.9 ± 1.0 (4.7 ± 0.5)	19.8 ± 3.2 (19.8 ± 3.2)
573 K (300 °C)-Tempered	61.4 ± 3.9 (74.9 ± 2.7)	17.7 ± 1.5 (4.2 ± 0.3)	20.9 ± 2.4 (20.9 ± 2.4)

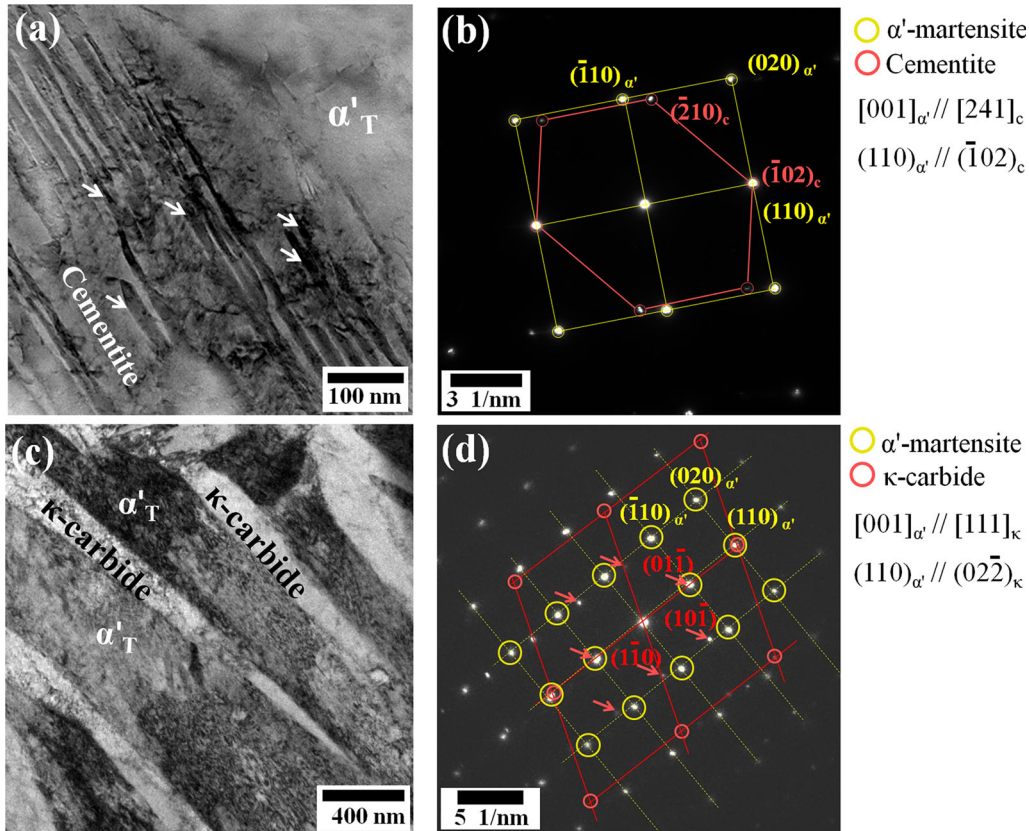( ): volume fraction measured after tensile test.

Fig. 3—(a) TEM brightfield image of thin cementite platelets inside α'-martensite and (b) selected area diffraction (SAD) patterns of cementite and α'-martensite in 373 K (100 °C)-tempered specimen. (c) TEM brightfield image of relatively coarse κ-carbide platelets inside α'-martensite and (d) SAD patterns of κ-carbide and α'-martensite in 573 K (300 °C)-tempered specimen.

thick and 1-2 μm long for the 573 K (300 °C)-tempered specimen.

To identify the platelets in martensite laths, both TEM analysis of the crystal structure and APT analysis of atomic-scale composition were performed using 373 K (100 °C)- and 573 K (300 °C)-tempered specimens. Figure 3 shows TEM brightfield images of two tempered specimens (Figures 3(a) and (c)) and selected area diffraction (SAD) patterns, which were taken from the [001] zone axis of the bcc structure (Figures 3(b) and (d)). Unlike the SAD patterns of κ-carbide and κ'-intermetallic precipitate in Fe-Mn-Al-C steels,[10–13,19–24] the SAD pattern of platelets in the 373 K (100 °C)-tempered specimen exhibited no superlattice spots, matching the pattern of cementite (Figure 3(b)). Accordingly,

the platelets in the 373 K (100 °C)-tempered specimen are thought to be cementite and no other types of precipitates were observed. The orientation relationship between martensite matrix and cementite is $(110)_{\alpha'}//(\bar{1}02)_c$ and $[001]_{\alpha'}//[241]_c$.

Meanwhile, the SAD pattern of platelets in the 573 K (300 °C)-tempered specimen exhibited superlattice spots (red arrows in Figure 3(d)), matching the pattern of κ-carbide (Figure 3(d)). Accordingly, the platelets in the 573 K (300 °C)-tempered specimen are thought to be κ-carbide, which has a specific orientation relationship with the martensite matrix, $(110)_{\alpha'}//(02\bar{2})_\kappa$ and $[001]_{\alpha'}//[111]_\kappa$. The TEM results of precipitates indicate that the transition from cementite to κ-carbide occurred with increase of tempering temperature from 373 K (100 °C)
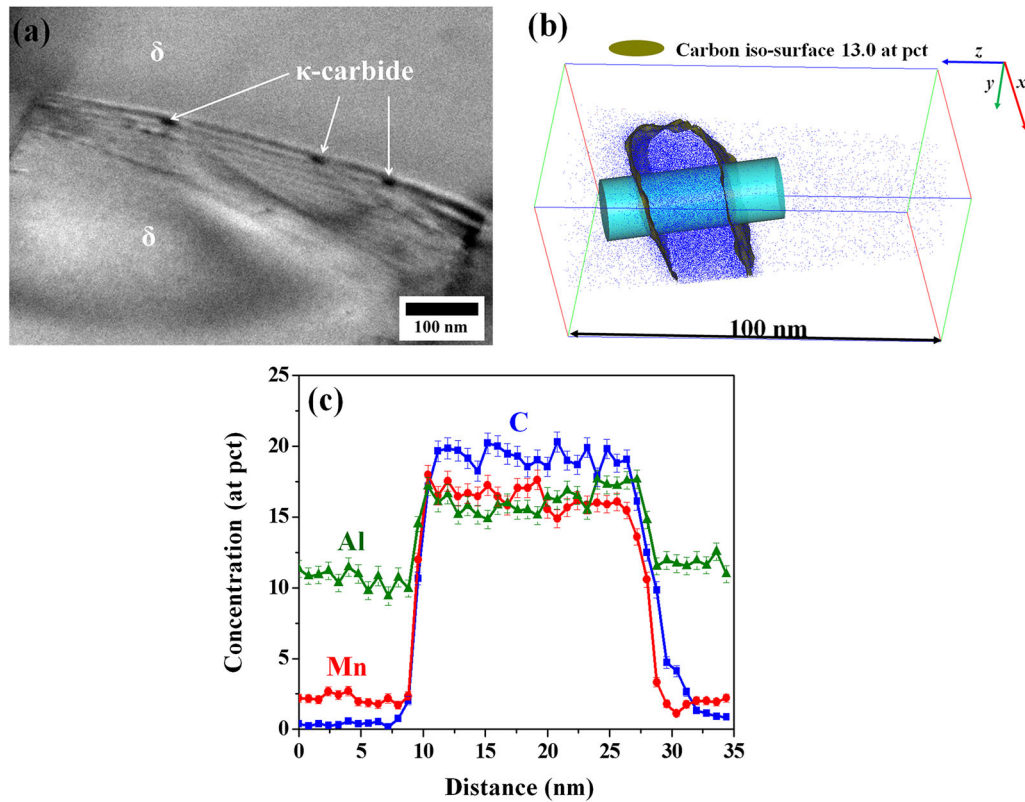
Fig. 4—(a) High-resolution TEM image of fine κ-carbide particles formed at ferrite grain boundaries of 573 K (300 °C)-tempered specimen. (b) Reconstructed APT map of C concentration, and (c) 1D concentration profiles of alloying elements in ferrite matrix and κ-carbide.

to 573 K (300 °C), which is different from thermodynamically predicted precipitation behavior (Figure 1).

In the case of the 573 K (300 °C)-tempered specimen, not only κ-carbide platelets in martensite laths but also other fine precipitates were observed in the grain boundaries of ferrite (Figure 4(a)). Due to the difficulty of obtaining a clear SAD pattern of the fine particles, APT experiments were conducted using the 573 K (300 °C)-tempered specimen. The fine particles with diameter of ~ 20 nm detected inside ferrite (Figure 4(b)) were enriched with Al as well as Mn and C (Figure 4(c)), which is indicative of κ-carbide. Therefore, it was realized that the 573 K (300 °C)-tempered specimen had coarse κ-carbide platelets in α'_T and fine κ-carbide particles at grain boundaries of ferrite.

In addition, decomposition of precipitates in the martensite matrix of the 573 K (300 °C)-tempered specimen was observed (Figure 5). Considering that the transition from cementite to κ-carbide occurred during tempering at 573 K (300 °C), it is thought that Figure 5 shows the decomposition of cementite.

Room-temperature engineering stress–strain curves and tensile properties of annealed and tempered specimens are shown in Figure 6(a). The annealed specimen underwent premature failure, exhibiting low strength and poor El (less than 2 pct). However, when the annealed specimen was tempered at 373 K (100 °C), YS, UTS, and El dramatically increased to 945 MPa, 1.56 GPa, and 16.8 pct, respectively. With further increase in the tempering temperature, both YS and

UTS decreased without significant reduction in El. Based on the strain-hardening rates (SHR), modified Cruassard-Jaoul (C-J) plots[42] of annealed and tempered specimens were drawn and are shown in Figure 6(b). The annealed specimen exhibited extremely high SHR until premature failure. The SHR of the tempered specimens decreased with the increasing tempering temperature. Of the tempered specimens, the 373 K (100 °C)-tempered specimen possessed high SHR, resulting in both ultrahigh UTS and moderate El.

To investigate the difference in SHR between annealed and tempered specimens, the fractions of retained austenite were measured by XRD after tensile tests and compared with those measured before tensile tests (Figure 6(c)). An almost identical fraction (~ 10 pct) of austenite was reduced by transformation to martensite during tensile tests in all specimens. In the case of the annealed specimen, the decrease of ~ 10 pct austenite fraction occurred readily at the early deformation, leading to extremely high SHR until El (~ 1.7 pct). This indicates that retained austenite in the annealed specimen is mechanically unstable at room temperature.

To investigate the behaviors of TRIP and fracture in the annealed specimen, the normal surface of annealed specimen was observed before and after tensile testing using the SEM-EBSD. In the undeformed annealed specimen, retained austenite grains formed near ferrite most likely due to C enrichment (Figure 7(a)). In the fractured specimen, cracks were observed. The cracks
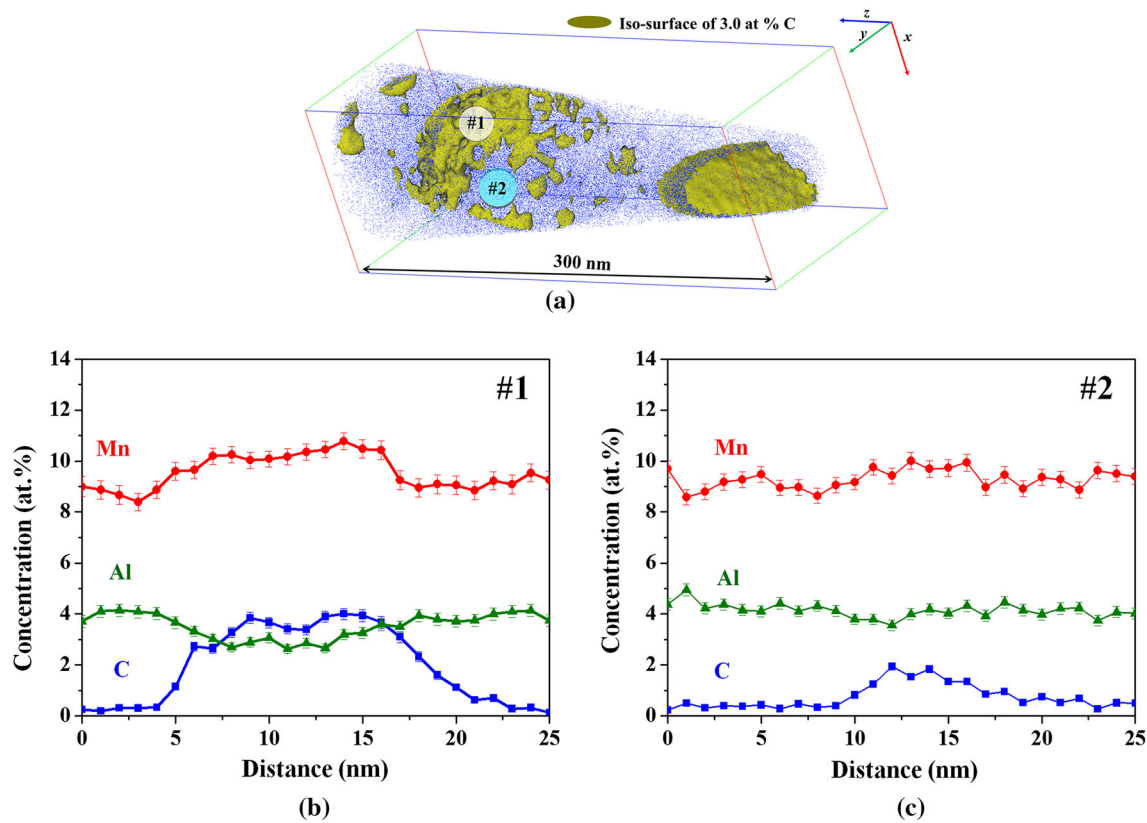
Fig. 5—(a) Reconstructed APT map of C concentration in martensite of 573 K (300 °C)-tempered specimen. 1D concentration profiles of alloying elements in (b) location #1 and (c) location #2 in (a).

were initiated at the junctions of ferrite and prior austenite grain boundaries, propagating along austenite grain boundaries (Figures 7(b-d)). This resulted in premature failure by brittle intergranular fracture (Figure 7(e)). Meanwhile, the low YS (~560 MPa) of the annealed specimen is thought to be influenced by both austenite and ferrite, considering that their hardness values are similar before tensile tests (Table III). However, the high SHR after yielding, caused by TRIP phenomenon as mentioned above, indicates that the low YS probably resulted from the stress-induced martensitic transformation of austenite due to its low stability.[43]

Meanwhile, the reason that the tensile properties of tempered specimens were greatly improved compared to the annealed specimen was analyzed from the following two points of view: TRIP and precipitation. To elucidate the TRIP behavior occurring during tensile deformation in the 373 K (100 °C)-tempered specimen, EBSD phase maps were obtained using tensile specimens deformed with various strains (Figure 8). Retained austenite gradually changed to martensite with increasing strain up to 12 pct; particularly large blocky austenite grains (white arrow in Figure 8(e)) were first transformed to martensite. As a result, the volume fraction of austenite (V_γ) decreased to 4.1 pct after tensile strain of 12 pct. This indicates that in the 373 K (100 °C)-tempered specimen TRIP occurs slowly and steadily with increase in strain, which is different from

the rapid TRIP observed in the annealed specimen. The gradual TRIP behavior resulted probably from austenite stabilized by C partitioning from martensite during tempering at 373 K (100 °C).

To confirm the C enrichment in austenite, the hardness values of each phase in both the annealed and tempered specimens were measured (Table III). The hardness value of martensite was highest in the annealed specimen and then decreased with increases in tempering temperature. On the other hand, the hardness value of austenite was lowest in the annealed specimen, and then increased with increasing tempering temperature. This implies that C partitioning from martensite to austenite occurred during tempering. To quantitatively evaluate the C partitioning, the C concentrations of retained austenite in the annealed and tempered specimens were measured using austenite lattice parameters (a_γ) obtained from XRD peaks and the following equation[44]:

$$a_\gamma(\text{Å}) = 3.578 + 0.0330 X_C + 0.0056 X_{Al} + 0.00095 X_{Mn},$$
[1]

where X_C, X_{Mn}, and X_{Al} are the concentrations (wt pct) of C, Mn, and Al in austenite, respectively. X_{Mn} and X_{Al} were measured by APT using the 573 K (300 °C)-tempered specimen and, because neither Mn nor Al can actively diffuse at temperatures less than 300 °C, these values are assumed to be the same in the annealed,
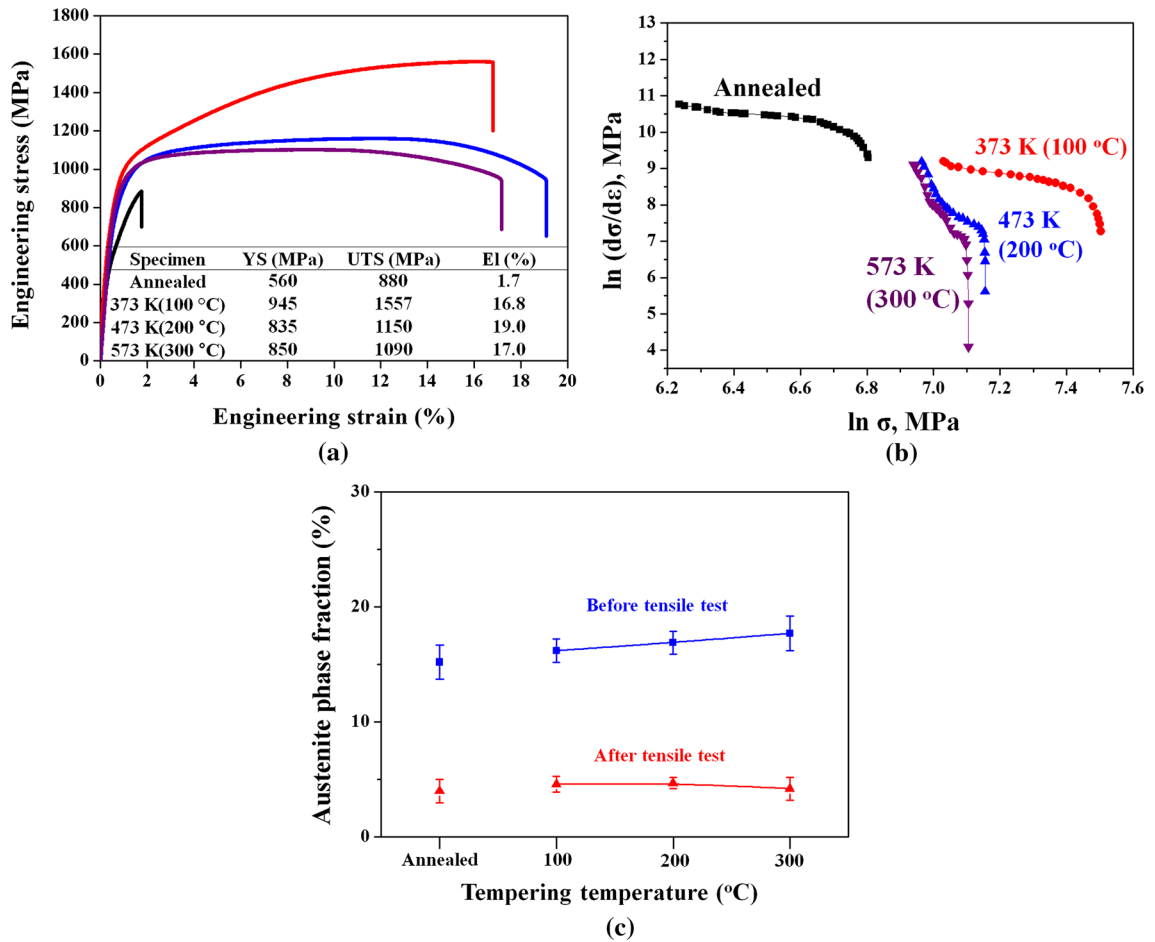
Fig. 6—(a) Engineering stress vs strain curves and tensile properties and (b) modified C–J plots of annealed and tempered specimens. With increasing tempering temperature, YS, UTS, and SHR decreased without significant reduction of El. (c) Volume fraction of retained austenite (Vγ) before and after tensile tests.
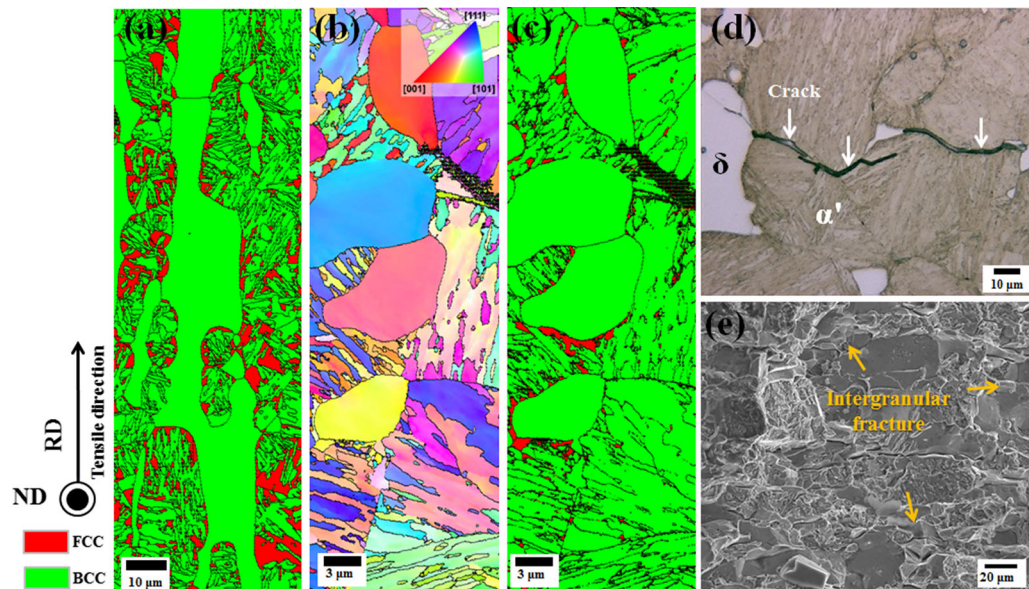

Fig. 7—(a) EBSD phase map of annealed specimens before tensile testing. (b) EBSD IPF map and (c) phase map of annealed specimen after tensile fracture. (d) Optical micrographs showing cracks on the normal surface near fracture tip and (e) fracture surface of annealed specimen.

Table III. Vickers Hardness Values of Martensite, Austenite, and Ferrite Phases in Annealed and Tempered Specimens Before Tensile Tests

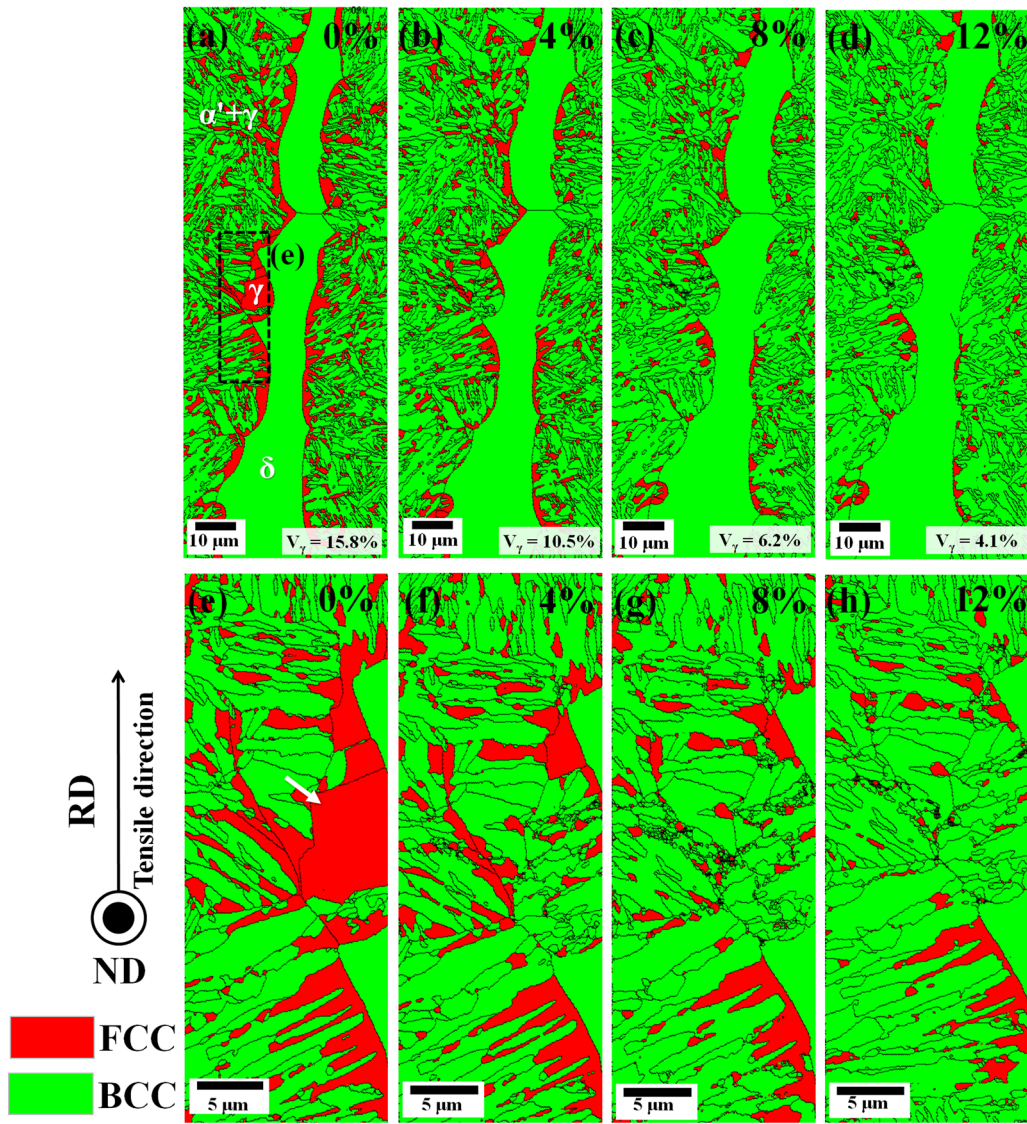| Specimen	Vickers Hardness (Hv)		
	Martensite	Austenite	Ferrite
Annealed	494.4 ± 26.7	212.6 ± 27.2	223.0 ± 10.1
373 K (100 °C)-Tempered	489.6 ± 27.2	293.7 ± 32.0	221.9 ± 6.8
473 K (200 °C)-Tempered	453.1 ± 42.3	314.5 ± 12.4	218.8 ± 9.4
573 K (300 °C)-Tempered	448.7 ± 31.8	310.1 ± 10.7	220.7 ± 12.2

Fig. 8—(a–d) EBSD phase maps of 373 K (100 °C)-tempered specimens deformed with various tensile strains until 12 pct. (e–h) High-magnified EBSD phase maps showing microstructural evolution, with tensile strain in dashed rectangular area in (a). Tensile strain is shown in the upper right corner of each map. Volume fraction of retained austenite (Vγ) is shown at the bottom of each map. With the increasing tensile strain, Vγ decreased gradually; large blocky austenite grains first changed to martensite.

373 K (100 °C)-, and 473 K (200 °C)-tempered specimens. It was found that X_C increased from 0.17 wt pct in the annealed specimen to 0.47 wt pct in the 573 K (300 °C)-tempered specimen (Table IV). The C enrichment in retained austenite by tempering made austenite hard (Table III), resulting in an increase in YS (Figure 6(a)). In addition, the hard austenite enriched with C was stabilized so that after yielding, soft ferrite

Table IV. Carbon Concentration of Retained Austenite in Annealed and Tempered Specimens

Specimen	C Concentration of Retained Austenite (Weight Percent)
Annealed	0.17
373 K (100 °C)-Tempered	0.36
473 K (200 °C)-Tempered	0.39
573 K (300 °C)-Tempered	0.47

C concentrations were measured using austenite lattice parameters (a_γ) obtained from XRD patterns and Eq. [1].[44]
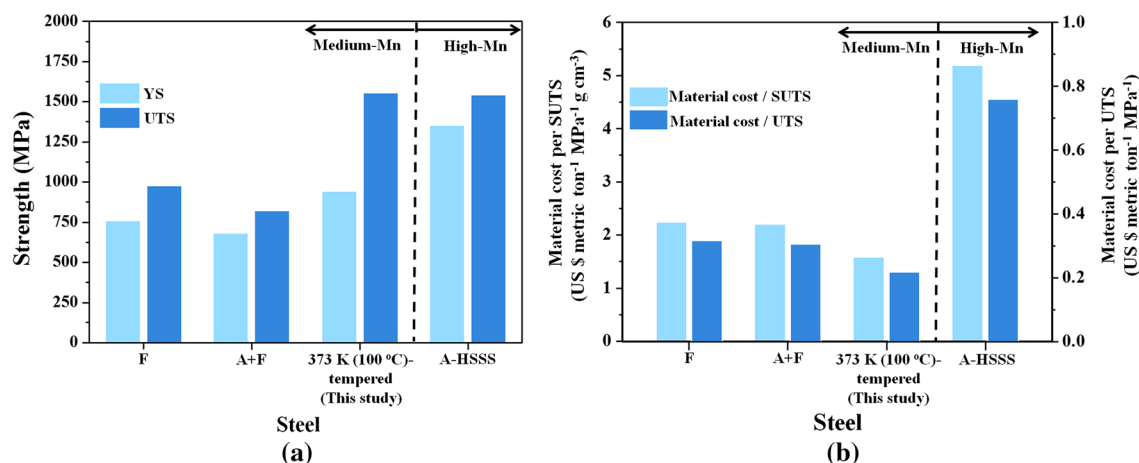

Fig. 9—Comparisons of (*a*) YS and UTS and (*b*) material cost per SUTS and material cost per UTS between various medium-[21,28] and high-Mn[20] lightweight steels with almost identical El of ~ 20 pct. F and A + F denote medium-Mn lightweight steels with ferrite and austenite + ferrite matrices, respectively. A-HSSS denotes austenitic high specific strength steel.

was first deformed, and TRIP in austenite occurred gradually. Accordingly, compared to the annealed specimen that showed rapid TRIP, tempered specimens exhibited low SHR, delayed cracking, and improved El.

Meanwhile, the difference in SHR values with the changing tempering temperature in tempered specimens is thought most likely to be due to the difference in precipitation behavior, because all tempered specimens similarly revealed gradual TRIP behavior. As seen in Figure 3(a), when tempering temperature was 373 K (100 °C), cementite platelets of 15-30 nm thickness formed, with interspacing of 10-20 nm in α'_T. When tempering temperature was 573 K (300 °C), preexisting cementite platelets were replaced by κ-carbide platelets of 150-200 nm thickness and an interspacing of 400-500 nm (Figure 3(c)). This coarsening of precipitates, as well as the depletion of C in α'_T, caused decreases in both the hardness of α'_T (Table III) and SHR, resulting in the decrease of UTS with increasing tempering temperature.

Figure 9(a) shows YS and UTS of medium- and high-Mn lightweight steels with almost identical El of ~ 20 pct. The strengths of the 373 K (100 °C)-tempered specimen are the highest among medium-Mn steels, and comparable to those of high-Mn austenitic steel (Austenite-High Specific Strength Steel, A-HSSS), which is currently known as the strongest lightweight steel. In addition, compared to A-HSSS (Fe-16.1Mn-9.6Al-0.86C-4.9Ni), the 373 K (100 °C)-tempered specimen possesses a small quantity of alloying elements

(Fe-8.8Mn-5.1Al-0.31C); accordingly, its low material cost is expected. Material cost per UTS and material cost per SUTS[45] of medium-Mn and high-Mn lightweight steels are compared in Figure 9(b). Values were calculated based on the average prices of alloying elements over the past 5 years (2013-2017) (https://www.kores.net). The 373 K (100 °C)-tempered specimen exhibits the lowest material cost per UTS and lowest material cost per SUTS among all lightweight steels.

IV. CONCLUSIONS

In the present study, a new alloy design was performed to develop an ultrahigh-strength (UTS > 1.5 GPa) medium-Mn lightweight steel with martensitic matrix. The Fe-8.8Mn-5.1Al-0.31C (wt pct) specimen, annealed at 1373 K (1100 °C) for 15 minutes, possessed a triple-phase microstructure composed of martensite, retained austenite, and ferrite. After tempering at 373 K (100 °C), thin cementite platelets formed with nanosized interspacing in α'_T. The tempered martensitic lightweight steel had ultrahigh UTS (~ 1.56 GPa); this value greatly exceeded the UTS (< 1.0 GPa) of previous medium-Mn lightweight steels and reached the UTS (~ 1.55 GPa) of high-Mn A-HSSS, which is currently the strongest lightweight steel. In addition, because the new steel contains a smaller amount of alloying elements than A-HSSS, its material cost per UTS and material cost per SUTS are the lowest among all lightweight

steels. The present martensitic lightweight steel will meet the strong demand for ultrahigh-strength lightweight steel for next generation vehicles.

DATA AVAILABILITY

The authors confirm that the data supporting the findings of this study are available within the article and its supplementary materials.

REFERENCES

1. B.C. De Cooman: *Curr. Opin. Solid State Mater. Sci.*, 2004, vol. 8, pp. 285–303.
2. G.K. Tirumalasetty, M.A. Van Huis, C. Kwakernaak, J. Sietsma, W.G. Sloof, and H.W. Zandbergen: *Acta Mater.*, 2012, vol. 60, pp. 1311–21.
3. P.J. Gibbs, E. De Moor, M.J. Merwin, B. Clausen, J.G. Speer, and D.K. Matlock: *Metall. Mater. Trans. A*, 2011, vol. 42, pp. 3691–3702.
4. G.-H. Kang, S. Duan, S.-J. Kim, and W. Bleck: *Metall. Mater. Trans. A*, 2016, vol. 47A, pp. 1918–21.
5. O. Bouaziz, S. Allain, C.P. Scott, P. Cugy, and D. Baribier: *Curr. Opin. Solid State Mater. Sci.*, 2011, vol. 15, pp. 141–68.
6. I. Gutierrez-Urrutia and D. Raabe: *Acta Mater.*, 2011, vol. 59, pp. 6449–62.
7. G. Frommeyer and U. Brüx: *Steel Res. Int.*, 2006, vol. 77, pp. 627–33.
8. K.-T. Park, K.G. Jin, S.H. Han, and S.W. Hwang: *Mater. Sci. Eng. A*, 2010, vol. 483, pp. 184–87.
9. K.-T. Park: *Scr. Mater.*, 2013, vol. 68, pp. 375–79.
10. K. Choi, C.-H. Seo, H. Lee, S.K. Kim, J.-H. Kwak, K.G. Chin, K.-T. Park, and N.J. Kim: *Scr. Mater.*, 2010, vol. 63, pp. 1028–31.
11. K.M. Chang, C.G. Chao, and T.F. Liu: *Scr. Mater.*, 2010, vol. 63, pp. 162–65.
12. C.L. Lin, C.G. Chao, H.Y. Bor, and T.F. Liu: *Mater. Trans. JIM.*, 2010, vol. 51, pp. 1084–88.
13. C.L. Lin, C.G. Chao, J.Y. Juang, J.M. Yang, and T.F. Liu: *J. Alloys Compd.*, 2014, vol. 586, pp. 16–20.
14. I. Gutierres-Urrutia and D. Raabe: *Acta Mater.*, 2012, vol. 60, pp. 5791–5802.
15. I. Gutierres-Urrutia and D. Raabe: *Mater. Sci. Technol.*, 2014, vol. 30, pp. 1099–1104.
16. H. Springer and D. Raabe: *Acta Mater.*, 2012, vol. 60, pp. 4950–59.
17. I. Gutierres-Urrutia and D. Raabe: *Scr. Mater.*, 2013, vol. 68, pp. 343–47.
18. E. Welsch, D. Ponge, S.M.H. Haghighat, S. Sandlobes, P. Choi, M. Herbig, S. Zaefferer, and D. Raabe: *Acta Mater.*, 2016, vol. 116, pp. 188–99.
19. Y. Satou, M. Kamiya, R. Umino, I. Ohnuma, and K. Ishida: *ISIJ Int.*, 2010, vol. 50, pp. 893–99.
20. S.H. Kim, H. Kim, and N.J. Kim: *Nature*, 2015, vol. 518, pp. 77–88.
21. S.-Y. Shin, H. Lee, S.-Y. Han, C.-H. Seo, K. Choi, S. Lee, N.J. Kim, J.-H. Kwak, and K.-G. Chin: *Metall. Mater. Trans. A*, 2010, vol. 41A, pp. 138–48.
22. S.-Y. Han, S.-Y. Shin, H.-J. Lee, B.-J. Lee, S. Lee, N.J. Kim, and J.-H. Kwak: *Metall. Mater. Trans. A*, 2012, vol. 43A, pp. 843–53.
23. S.S. Sohn, B.-J. Lee, J.-H. Kwak, and S. Lee: *Acta Mater.*, 2013, vol. 61, pp. 5626–35.
24. S.S. Sohn, B.-J. Lee, J.-H. Kwak, and S. Lee: *Metall. Mater. Trans. A*, 2014, vol. 45A, pp. 3844–56.
25. S.S. Sohn, B.-J. Lee, and J.-H. Kwak: *Met. Mater. Int.*, 2015, vol. 21, pp. 43–53.
26. R.-C. Xu, Y.-L. He, H. Jiang, H. Wang, N.-Q. Zhu, X.-G. Lu, and L. Li: *J. Iron Steel Res. Int.*, 2017, vol. 24, pp. 737–42.
27. H. Song, S.G. Lee, S.S. Sohn, J.-H. Kwak, and S. Lee: *Metall. Mater. Trans. A*, 2016, vol. 47A, pp. 5372–92.
28. S.S. Sohn, B.-J. Lee, S. Lee, N.J. Kim, and J.-H. Kwak: *Acta Mater.*, 2013, vol. 61, pp. 5050–66.
29. S.S. Sohn, K. Choi, J.-H. Kwak, N.J. Kim, and S. Lee: *Acta Mater.*, 2014, vol. 78, pp. 181–89.
30. C.-H. Seo, K.H. Kwon, K. Choi, K.-H. Kim, S. Lee, and N.J. Kim: *Scr. Mater.*, 2012, vol. 66, pp. 519–22.
31. S.S. Sohn, H. Song, J.G. Kim, J.-H. Kwak, H.-S. Kim, and S. Lee: *Metal. Mater. Trans. A*, 2016, vol. 47A, pp. 706–17.
32. S.S. Sohn, S. Lee, B.-J. Lee, and J.-H. Kwak: *JOM*, 2014, vol. 66, pp. 1857–67.
33. J. Park, M.C. Jo, H.J. Jeong, S.S. Sohn, J.-H. Kwak, H.S. Kim, and S. Lee: *Sci. Rep.*, 2017, vol. 7, p. 15726.
34. S.S. Sohn, H. Song, J.-H. Kwak, and S. Lee: *Sci. Rep.*, 2017, vol. 7, p. 1927.
35. H. Song, S.S. Sohn, J.-H. Kwak, B.-J. Lee, and S. Lee: *Metal. Mater. Trans. A*, 2016, vol. 47A, pp. 2674–85.
36. C.-Y. Lee, J. Jeong, J. Han, S.-J. Lee, S. Lee, and Y.-K. Lee: *Acta Mater.*, 2015, vol. 84, pp. 1–8.
37. J. Jeong, C.-Y. Lee, I.-J. Park, and Y.-K. Lee: *J. Alloys Compd.*, 2013, vol. 574, pp. 299–304.
38. S. Lee, J. Jeong, and Y.-K. Lee: *J. Alloys Compd.*, 2015, vol. 648, pp. 149–53.
39. J. Mahieu, J. Maki, B.C. De Cooman, and S. Claessens: *Metall. Mater. Trans. A*, 2002, vol. 33A, pp. 2573–80.
40. Thermo-Calc. Database TCFE2000, upgraded by Lee, B.-J. & Sundman, B., Stockholm., KTH, 1999.
41. K.-G. Chin, H.-J. Lee, J.-H. Kwak, J.-Y. Kang, and B.-J. Lee: *J. Alloys Compd.*, 2010, vol. 505, pp. 217–23.
42. J.E. Jin and Y.-K. Lee: *Acta Mater.*, 2012, vol. 60, pp. 1680–88.
43. D. Fahr: *Metall. Trans.*, 1971, vol. 2, pp. 1883–92.
44. S.S. Babu, E.D. Specht, S.A. David, E. Karapetrova, P. Zschack, M. Peet, and H.K.D.H. Bhadeshia: *Metall. Mater. Trans. A*, 2005, vol. 36A, pp. 2005–3281.
45. M.A. Maleque and S. Dyuti: *Int. J. Mech. Mater. Eng.*, 2010, vol. 5, pp. 95–100.